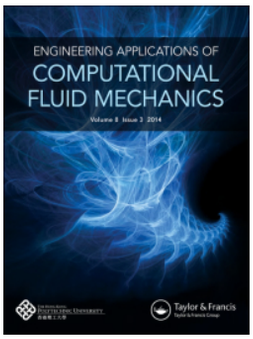

Taylor & Francis
Taylor & Francis Group

Engineering Applications of Computational Fluid Mechanics

ISSN: (Print) (Online) Journal homepage: https://www.tandfonline.com/loi/tcfm20

Study on mathematical model construction of typical gorge wind field

Jionghao Cheng, Zhenxu Sun, Shengjun Ju, Guowei Yang, Jun Mao & Dilong Guo

To cite this article: Jionghao Cheng, Zhenxu Sun, Shengjun Ju, Guowei Yang, Jun Mao & Dilong Guo (2023) Study on mathematical model construction of typical gorge wind field, Engineering Applications of Computational Fluid Mechanics, 17:1, 2249132, DOI: 10.1080/19942060.2023.2249132

To link to this article: https://doi.org/10.1080/19942060.2023.2249132

Published online: 23 Aug 2023.

ENGINEERING APPLICATIONS OF COMPUTATIONAL FLUID MECHANICS
2023, VOL. 17, NO. 1, 2249132
https://doi.org/10.1080/19942060.2023.2249132

Taylor & Francis
Taylor & Francis Group

Study on mathematical model construction of typical gorge wind field

Jionghao Cheng[a,b], Zhenxu Sun[a], Shengjun Ju[a], Guowei Yang[a], Jun Mao[c] and Dilong Guo[a]

[a]Key Laboratory for Mechanics in Fluid Solid Coupling Systems, Institute of Mechanics, Chinese Academy of Sciences, Beijing, People's Republic of China; [b]School of Engineering Sciences, University of Chinese Academy of Sciences, Beijing, People's Republic of China; [c]School of civil engineering, Beijing Jiaotong University, Beijing, People's Republic of China

ABSTRACT

Wind conditions in gorges have a significant impact on the safe operation of high-speed trains, due to the lack of a unified gorge wind model and the limitations of traditional simulations that use oversimplified wind models, the complex wind speed distribution arising from the mountain surface boundary layer cannot be accurately captured. To address this, a three-dimensional, incompressible, steady calculation method is used to study wind field characteristics in a typical gorge. We propose a two-dimensional mathematical model to study the effects of gorge width on model parameters, including wind speed growth indices α_1 and α_2 in the height and horizontal directions, respectively. Our results demonstrate that the thickness of the mountain boundary layer can reach a maximum of approximately 30 metres, and the values of α_1 and α_2 range from 0.11 to 0.19 and 0.21 to 0.5, respectively. As gorge width increases, boundary layer thickness remains constant, α_1 gradually decreases, α_2 remains unchanged above 250 m height. Our findings provide more accurate boundary conditions for numerical simulations of high-speed train operation in gorge wind conditions and offer theoretical recommendations for safe high-speed train operation through bridges, tunnels, and railways in mountainous regions.

ARTICLE HISTORY
Received 7 March 2023
Accepted 12 August 2023

KEYWORDS
Wind field characteristics; mathematical model; roughness; numerical simulation; wind speed fitting

Symbol description

symbol	definition	unit
ρ	fluid density	kg/m³
t	time	s
u_i	velocity in the x-direction	m/s
u_j	velocity in the y-direction	m/s
u_k	velocity in the z-direction	m/s
x_i	x-coordinate	m
x_j	y-coordinate	m
μ	dynamic viscosity coefficient	Pa·s
δ_{ij}	Kronecker symbol	
K	thermal conductivity coefficient	W/(m·K)
T	temperature	K
γ	specific heat ratio	
R	gas constant	J/(mol·K)
e	specific internal energy of a unit mass of gas	m^2/s^2
y_0	roughness length	m
r	physical roughness height	m
u	velocity	m/s
κ	von Karman constant	
u^*	reference velocity	m/s
ν	kinematic viscosity coefficient	m^2/s
E	default constant	
E'	segmented function	
y	distance from the centre of the grid to the wall	m
f	roughness function	
R^+	$R^+ = ru^*/\nu$	
R^+_{smooth}	default parameter	
R^+_{rough}	default parameter	
B	default parameter	
C	default parameter	
h	height of the gorge	m
U	wind speed	m/s
U_0	wind speed at the gradient wind height	m/s
z	height above the ground	m
H_g	gradient wind height	m
α	surface roughness index	
y	y-coordinate	
$U(z)$	distribution of wind speed in the vertical direction of the gorge	m/s
U_h	wind speed at the mountain's highest point	m/s
z	z-coordinate	m

CONTACT Dilong Guo jack9517@126.com

α_1	wind speed increase index in the height direction	
$U(x)$	distribution of wind speed in the horizontal direction of the gorge	m/s
U_{max}	maximum wind speed at a specific height	m/s
x_0	interval of wind speed growth along the horizontal direction near the mountain wall	m
α_2	wind speed increase index in the horizontal direction	
$U(x, z)$	two-dimensional wind profile	m/s

1. Introduction

The total area of mountainous lands in the western China is about 4 million square kilometres, accounting for 65% of the total mountainous area in China (Tan, 2019). Large-scale building of high-speed rail in mountainous regions with precarious gorges has begun in response to the implementation of the western development strategy. Trains operating in such environments must contend with more complex and unpredictable gorge wind loads due to the mountainous terrain's complicated topography and abundance of gorges. Vehicle stability when exposed to crosswind is one of the priorities in bridge design (He et al., 2022). In addition to serving as the foundation for bridge wind resistance design (Li et al., 2010), the research of gorge wind field characteristics also serves as a guarantee for the safe operation of trains. Deep-cut gorges have accelerating and limiting effects on incoming flow, making the spatial distribution characteristics of canyons wind fields anisotropic (Zhang et al., 2021). Strong winds can even increase the likelihood of train derailments and overturning in windy sections of the mountains (Zou et al., 2022), especially when the train enters and exits the tunnel frequently in a short period of time under gorge wind loads. Due to the sudden changes in the train operating environment, compression waves and expansion waves are generated during train operation and the vortex structure on the leeward side of the train also changes drastically, resulting in extremely complex flow around the train. While the conventional study of train operation in cross wind is not accurate enough for the setting of wind field boundary conditions, so it is imperative to explore a more realistic gorge wind model to provide more exact boundary conditions for the numerical simulation of train operations in the gorge area.

In the field of wind engineering, there has been a growing interest in studying wind field characteristics in complex terrain, which has been driven by field measurements, numerical simulations, and experimental research conducted in wind tunnels (Shen et al., 2020). In terms of field measurements, Davenport and Kaimal measured wind characteristic parameters at various heights and locations, and respectively proposed the Davenport spectrum and Kaimal spectrum by analyzing of the measured results (Davenport, 1962; Kaimal et al., 1972). Similarly, Pang et al. (2010) measured the wind field at the Si Du River Bridge, calculated the mean wind speed, corresponding wind direction, turbulence intensity, gust factor and turbulence characteristics for a 10-minutes time-averaged sample, and fitted the pulsating wind power spectrum; Ke and Pei (2022) based on a typical U-shaped canyon located in the western mountainous area, the average wind characteristics and turbulence characteristics of the canyon were obtained through long-term wind field measurements. The measured results can provide reference for the study of wind fields in mountainous areas.

Although field measurements can yield the most accurate results, they are time-consuming, labor-intensive, and only allow for the collection of a limited number of fixed locations. In addition, the terrain in the gorge is highly intricate, which makes it challenging to quantify wind speeds within the mountains (Xue & Liu, 2016). Wind tunnel tests are also an important method that utilize scaled models to evaluate wind characteristic parameters at the bridge location. Taylor and Teunissen (1987) used three different scaling ratios (1:800, 1:1200, and 1:2500) to conduct wind tunnel tests of the wind field on the Askervein hill's wind field characteristics. By comparing the results to the measured data, it was discovered that the experimental error of the mean wind speed was small, while the experimental error of the turbulence statistics was larger. This proves that the wind tunnel tests are accurate in simulating the mean wind speed. Li et al. (2016) created different types of single mountain models for testing and investigated the effects of slope, height and the mountain shape on the topographic correction coefficients of wind speeds at different locations on the mountain. Aiming at complex ski resorts in mountainous areas, Zhao (2021) conducted wind tunnel experiments to finely describe the wind field characteristics of the canyon from the perspectives of both mean wind characteristics and turbulence characteristics. Nevertheless, terrain wind tunnel tests still have some disadvantages, such as long testing periods, limited experimental conditions, and high costs.

As computational fluid dynamics (CFD) advances by leaps and bounds, numerical simulation has gained increasing attention in the study of wind fields in complex terrain due to its economy and convenience. Many

scholars have used numerical simulation to study wind field characteristics in real or ideal terrain. Li et al. (2016) took the real topography of the gorge with a large span suspension bridge as the background and employed the CFD method to explore the influence of the mountainous Y-shaped estuary on the mean wind speed, wind attack angle, wind profile, and wind speed amplification coefficient under different incoming flow directions. The Qingshui River Bridge in China is one such location, and Zhang et al. (2017) used numerical calculation to investigate basic wind parameters at the bridge site based on the deep gorge terrain. They concluded that wind-induced vibration calculation of the bridge only needs to take into account the effect of the wind attack angle within 6° of the incoming flow. These studies primarily focused on wind field characteristics of particular mountain bridges, but they neglected to take surface roughness into consideration while analyzing the flow field. Hong (2020) investigated the wind field characteristics of U-shaped and V-shaped canyons, as well as the impact of canyon parameters on the wind field, using numerical simulation methods. Other researchers have used roughness wall functions to simulate the wind field of rugged terrain (Deng et al., 2010; Di et al., 2017), but the majority of these studies focused on the wind velocity characteristics of particular mountain locations rather than the spatial wind velocity distribution characteristics inside the gorge.

High-speed trains often encounter strong crosswind when they run to the tunnel–bridge–tunnel infrastructure (Yang et al., 2021). In the numerical simulation of side-wind aerodynamic characteristics of high-speed trains, some scholars have adopted the uniform wind or exponential wind model of the atmospheric boundary layer as the boundary conditions (Xia et al., 2022; Zhou et al., 2023). While this setup is feasible in open-field conditions, the actual wind profile in gorge regions will no longer satisfy the exponential wind model due to the influence of the mountain and ground boundary layers (Li et al., 2011). This can have an impact on the computational results.

As China's high-speed railway network expands into mountainous areas, there will be a growing number of tunnels and bridges crossing high mountains and gorges. Frequent operations of high-speed trains in tunnels and on bridges in the presence of gorge winds will become commonplace, highlighting the need to investigate the accurate and realistic gorge wind field as a prerequisite for ensuring the safety of high-speed railway operations in these regions. This study aims to overcome limitations in measuring wind fields and conducting region-specific numerical simulations by developing mathematical models that accurately describe gorge wind fields. These models will facilitate safe high-speed train operations over bridges and tunnels in mountainous regions. First, a realistic three-dimensional model of Askervein Hill is created to check the accuracy of the numerical simulation algorithm and mesh strategy against measured wind speeds. Next, a typical gorge calculation model is constructed to evaluate wind field characteristics. Finally, a gorge wind field model is developed and compared to other models, leading to more precise boundary conditions and theoretical recommendations for safe high-speed train operation in mountainous regions.

2. Calculation method and model

2.1. Governing equations

The gorge wind field was computed using the commercial software STAR-CCM+, and the three-dimensional, incompressible, steady Navier-Stokes (N-S) equation was solved by the following control equation.

The continuity equation is:

$$\frac{\partial ui}{\partial xi} = 0 \tag{1}$$

The momentum conservation equation is:

$$\rho \frac{\partial}{\partial xi}(uiuj) = -\frac{\partial P}{\partial xi} + \frac{\partial}{\partial xj}\left[\mu\left(\frac{\partial ui}{\partial xj} + \frac{\partial uj}{\partial xi} - \frac{2}{3}\frac{\partial ui}{\partial xi}\delta ij\right)\right] \tag{2}$$

The energy conservation equation is:

$$\frac{\partial}{\partial xi}\left[ui\rho\left(e + \frac{1}{2}uiui\right) + uiP\right] = \frac{\partial}{\partial xj}\left[K\frac{\partial T}{\partial xj} + ui\mu\left(\frac{\partial ui}{\partial xj} + \frac{\partial uj}{\partial xi}\right) - \frac{2}{3}ui\mu\frac{\partial ui}{\partial xi}\delta ij\right] \tag{3}$$

$$e = \frac{P}{\rho(\gamma - 1)} + \frac{1}{2}(ui^2 + uj^2 + uk^2) \tag{4}$$

The equation of state for the whole gas must also be added to make the equation closed:

$$P = \rho RT \tag{5}$$

In equation (1)-(5), ρ, P, t are density, pressure and time respectively, x and u are coordinates and velocity respectively, the subscripts i, j and k denote the three directional components, δ_{ij} is the Kronecker sign, μ is the viscosity coefficient, e is the internal energy per unit mass of gas, K is the heat transfer coefficient, T is the temperature, γ is the specific heat ratio and R is the gas constant.

Table 1. Roughness lengths of different types of ground surfaces.

Examples	Roughness length (m)
Open sea, snow-covered flat plain	0.0002
Beaches, pack ice without large ridges	0.005
Level country with low vegetation	0.03
Dense shelterbelts, vineyards	0.25
Mature forests, cities or villages.	1

In existing research, the well-established and widely used turbulence models include the standard k-ε turbulence model and the SST k-ω model. Due to its inadequate handling of flow with adverse pressure gradients and separation regions, the Standard k-ε turbulence model is considered unsuitable for numerical simulations of flow around bluff bodies by some researchers (Murakami, 1993). Menter (1994) introduced the SST k-ω model, which effectively computes turbulent shear stress transport in adverse pressure gradient boundary layers and is regarded as one of the most suitable two-equation turbulence models for simulating separation in bluff body flows within Reynolds-Averaged Navier-Stokes (RANS) methods. In this study, following reference (Tang et al., 2014), the SST k-ω turbulence model was selected. The convective term in the equations was discretized using the Roe scheme, while the viscous term was discretized using a second-order central difference method.

2.2. Wall roughness

In numerical simulations of complex terrain, the velocity distribution at the ground surface is greatly influenced by surface roughness. Surface roughness can be described in two ways, with engineers most often using the roughness length $\mathbf{y_0}$, which is the height from the ground surface to the point in the near-ground layer where wind speed is zero (Deng et al., 2010). The second way to express surface roughness is through the physical roughness height r, which corresponds to the equivalent sand grain height in circular tube turbulence experiments. Table 1 (Wieringa, 1992) presents roughness lengths for different surface types, computed by researchers using long-term empirical wind field data. Several studies (Abdi & Bitsuamlak, 2014; Mao et al., 2011; Menter, 1994; Pattanapol et al., 2007; Zhou et al., 2008) have employed the wall function method to simulate roughness in complex terrain, and the simulation results have shown good agreement with actual measurements. Thus, in this paper, we also adopt the wall function method to simulate roughness.

When utilizing the wall function, two opposing conditions must be simultaneously satisfied (Blocken et al., 2007). It is therefore essential to appropriately set the roughness height and initial grid height of the wall. On one hand, the near-wall grid resolution must be sufficiently high to accurately capture the wall velocity distribution. On the other hand, the distance from the wall to the centre of the initial grid should be larger than the roughness height. Otherwise, if the centre of the first grid is lower than the roughness height, it is equivalent to dividing the grid on the solid wall in fluid space, resulting in the inability to compute and losing the physical meaning of roughness.

This paper employs the wall function to calculate the velocity around the wall, dividing it into a viscous bottom layer, a logarithmic layer, and a turbulent layer. The first grid layer is set to be within the logarithmic layer by default. Equation (6) shows the velocity distribution in the logarithmic layer.

$$\frac{u}{u^*} = \frac{1}{\kappa}\ln\left(E'\frac{yu^*}{\nu}\right) \tag{6}$$

$$E' = \frac{E}{f} \tag{7}$$

Where u is the velocity, κ is the von Karman constant (which takes the value of 0.42), u* is the reference velocity (which is derived from the turbulence volume of the turbulence model), ν is the kinematic viscosity coefficient, y is the distance from the centre of the grid to the wall, E is the default constant (which takes the value of 9), and f is the roughness function.

The dimensionless quantity R^+ is defined as $R^+ = ru^*/\nu$, where r is the physical roughness height. Additionally, the roughness function f is a segmented function (Cebeci & Bradshaw, 1977).

When $R^+ \le \mathrm{R}^+_{\mathrm{smooth}}$ ($\mathrm{R}^+_{\mathrm{smooth}}$ is a default parameter),

$$f = 1 \tag{8}$$

When $\mathrm{R}^+_{\mathrm{smooth}} < R^+ \le \mathrm{R}^+_{\mathrm{rough}}$ ($\mathrm{R}^+_{\mathrm{rough}}$, B and C are default parameters),

$$f = \left[\mathrm{B}\left(\frac{R^+ - \mathrm{R}^+_{\mathrm{smooth}}}{\mathrm{R}^+_{\mathrm{rough}} - \mathrm{R}^+_{\mathrm{smooth}}}\right) + CR^+\right]^a \tag{9}$$

Where the index a is defined as:

$$a = \sin\left[\frac{\pi}{2}\frac{\log(R^+/\mathrm{R}^+_{\mathrm{smooth}})}{\log(\mathrm{R}^+_{\mathrm{rough}}/\mathrm{R}^+_{\mathrm{smooth}})}\right] \tag{10}$$

When $R^+ > \mathrm{R}^+_{\mathrm{rough}}$,

$$f = \mathrm{B} + CR^+ \tag{11}$$

In addition, the relationship between the physical roughness height r and roughness length $\mathrm{y_0}$ in STAR-CCM + is

$$\mathrm{r} = \frac{E\mathrm{y_0}}{\mathrm{C}} \tag{12}$$

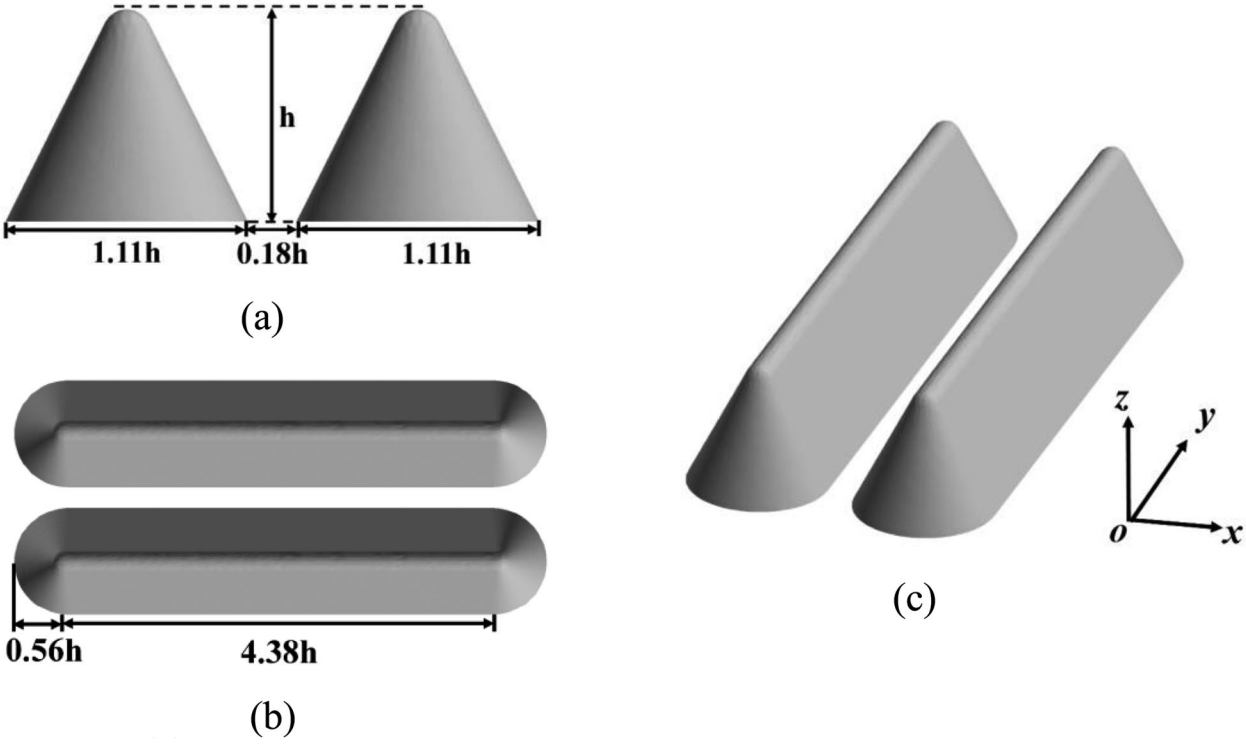

Figure 1. Gorge model. (a) Front view, (b) Vertical view, (c) Oblique view.

The values of default parameters in the equations are $B = 0, C = 0.253, R^{+}_{smooth} = 2.25, R^{+}_{rough} = 90$.

2.3. Computational model and domain

This paper takes the Sichuan-Tibet Railway as the background. The length of bridges on the Sichuan-Tibet Railway is mostly between 300m-500 m. There are many sections of the Yarlung Zangbo River valley with a typically long and straight shape, and the length is about 1km-5 km. Referring to this characteristic shape, we took the isosceles triangle as the cross-section of the mountain gorge, with rounded corners at the top of the mountain. The forward part of the mountain is made by rotating the triangular cross-section. The mountain's height, denoted as h, is 450 m. Taking h as the characteristic length, the mountain's length and width are 2.4 and 5.5 h respectively. The dimensions of the computational domain are 24.3 h in length, 13.2 h in width, and 6.7 h in height. The dimensions of the mountain and the calculation domain are shown in Figures 1 and 2.

2.4. Grid strategy

There are numerous surface types in the mountain, and the amount of vegetation that grows on the gorge's surface varies with the season. In order to fully consider the relationship between calculation accuracy and surface

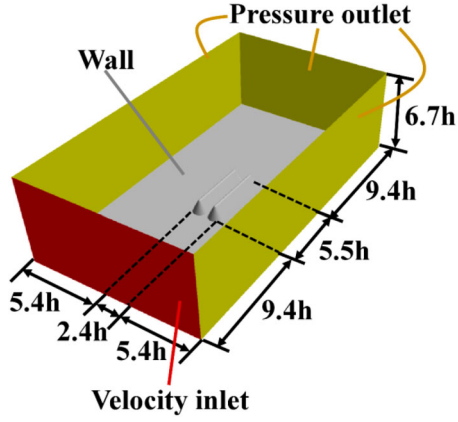

Figure 2. Schematic diagram of calculation domain.

roughness, the gorge studied in this paper is one with a shallow grass or low vegetation surface type and low roughness, and according to Equation (12), the roughness height is set to 1 m. This paper follows the roughness requirements specified in the literature (Blocken et al., 2007), with the first grid height of the boundary layer of the mountain wall set to 2 m, a grid growth rate of 1.1, and the outermost grid height of the boundary layer set to 10 m. Two refinement zones, where the grid size is smaller, were established near the gorge to better capture wind flow in this area. A refinement region was also established throughout the calculation domain to

Table 2. Four types of surface parameters.

Classification of surface	Height of gradient wind (m)	Roughness exponent
A (Sea, desert, etc.)	300	0.12
B (Fields, jungle, etc.)	350	0.16
C (Flat hilly area, etc.)	400	0.22
D (Rolling hills, etc.)	450	0.3

accommodate the exponential wind model, which uses a gradient wind height of 350 m for the velocity boundary condition. The specific grid sizes will be discussed in the subsequent grid independence analysis.

2.5. Boundary conditions

The boundary conditions of the simulation include velocity inlet, pressure outlet, and wall boundaries, as shown in Figure 2. The velocity inlet boundary is located in front of the gorge, and the atmospheric boundary layer exponential wind model, represented by Equation (13), is applied.

$$U = \mathrm{U}_0\left(\frac{z}{\mathrm{H_g}}\right)^{\alpha} \tag{13}$$

Where U_0 is the wind speed at the gradient wind height, which is set to 30 m/s, z is the height above the ground, $\mathrm{H_g}$ is the gradient wind height, and α is the roughness index. According to the wind resistance design specification for highway bridges, the inlet velocity model parameters follow the type B surface shown in Table 2 (Chen, 2022), with $\mathrm{H_g}$ set to 350 m and α set to 0.16. The pressure outlet boundary is set at the rear and both sides of the computational domain, the top of the computational domain is set as the symmetric boundary, and the gorge mountain is used as a rough wall boundary with a roughness height of 1 m.

3. Verification

3.1. Algorithm validation

The accuracy of the numerical algorithm and the roughness settings were verified by using the case of Askervein Hill, situated on the west coast of Scotland at a height of 116 m (126 m above sea level), with geographical coordinates of 57°11′16.63″N, 7°22′45.07″W. The International Energy Association conducted wind field empirical measurements in the area during 1982-1983, and the report of this project (Taylor & Teunissen, 1985) was used as a reference by atmospheric boundary layer researchers. An area of 4 km ∗ 4 km ∗ 1.5 km near the hill was selected as the calculation domain. The elevation data was obtained from the Chinese spatial geographic data cloud database, converted into point cloud data with 3D spatial coordinates by a coordinate converter, and reverse-engineered by 3D software to generate the hill's surface, as shown in Figure 3.

The ground roughness length y_0 of the hill is approximately 0.028 m, based on the local cover of grass as reported in (Deng et al., 2010; Di et al., 2017). The wall roughness height of the hill is set to 1 m, following the relationship between the physical roughness height r and roughness length y_0 in STAR-CCM + . The wall boundary layer meshing strategy from 2.2 is utilized to generate the volume mesh, with a maximum volume mesh of 40 m in space. The TU03B case is computed with a wind speed of 9.11 m/s (Tang et al., 2014; Taylor & Teunissen, 1985) and a wind direction of 30°N.E. at a height of 10 m, and the boundary conditions include velocity inlet and pressure outlet. The mesh and boundary conditions are illustrated in Figures 4 and 5.

The locations of the measurement points are depicted in Figure 6. In the actual measurement project, a large number of anemometers were erected on the A-A' line, and measurement points were situated close to the hill with reference to the location of the anemometers, all of which were 10 m above ground level, with point H being the highest point on the hill.

Figure 7 gives a comparison between the measured data and the numerical calculation results. The wind speed distribution obtained from the numerical calculations for the A-A' line is generally consistent with the measured data, indicating that the numerical calculation method, grid division strategy and roughness setting in this study were used reasonably. The surface of the mountain used in the CFD calculation has some deviations from the actual mountain due to the use of latitude and longitude data with 30 m accuracy. As a result, the measurement points in the numerical simulation do not correspond exactly to the measurement points in the measured data, and there are some errors in the wind speed calculated at certain locations. However, this does not affect the verification of the accuracy of the algorithm. In the next section, the same algorithm and boundary layer grid strategy will be used to investigate the wind field characteristics in a typical gorge.

3.2. Analysis of meshing independence

To verify the influence of grid resolution on computational accuracy, a grid independence study was conducted for the gorge model established in Section 2.3. The calculation method was consistent with that in Section 3.1, and the boundary conditions were consistent with those in Section 2.5. Under the premise of ensuring that the grid centre height of the first layer is higher than the roughness height, low, medium, and high-resolution grid models were established by adjusting the size of the

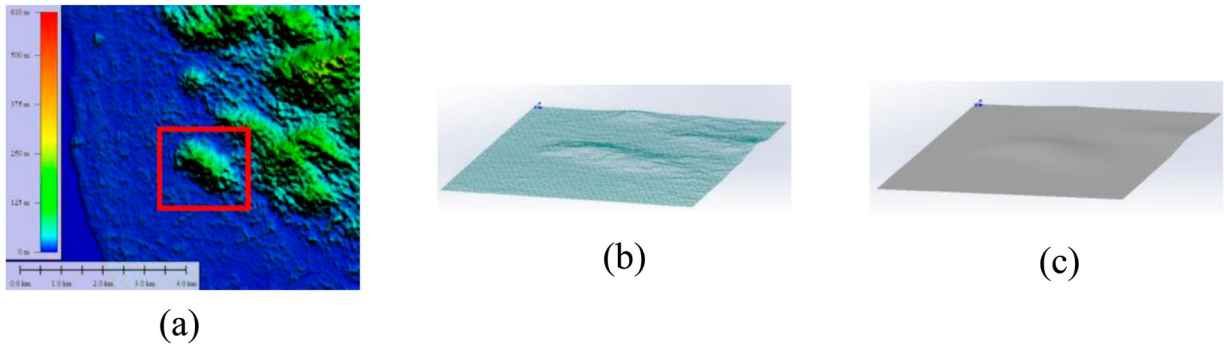

Figure 3. Formation process of Askervein hill. (a) Topographic map, (b) Point cloud, (c) Surface.

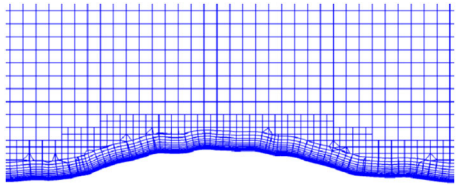

Figure 4. Local grid of Askervein hill.

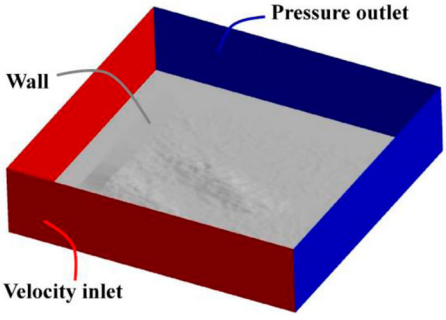

Figure 5. Schematic diagram of boundary.

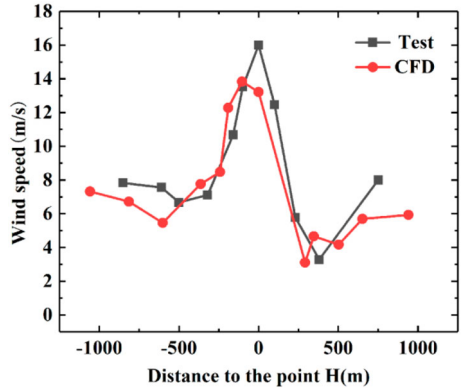

Figure 7. Comparison between calculated result and measured data

Table 3. Grid configuration of three grid models.

Grid resolution	Refinement zone 1	Refinement zone 2	Total number
Low	15m	30m	2 million
Medium	10m	20m	6 million
High	8m	16m	13 million

refinement region. The relevant grid configuration of the three sets of grid models is shown in Table 3, and the spatial distribution of the three grid models are illustrated in Figure 8.

A series of measurement points were arranged within 50 metres from the mountain wall at the entrance of the gorge. The measurement points were located at a

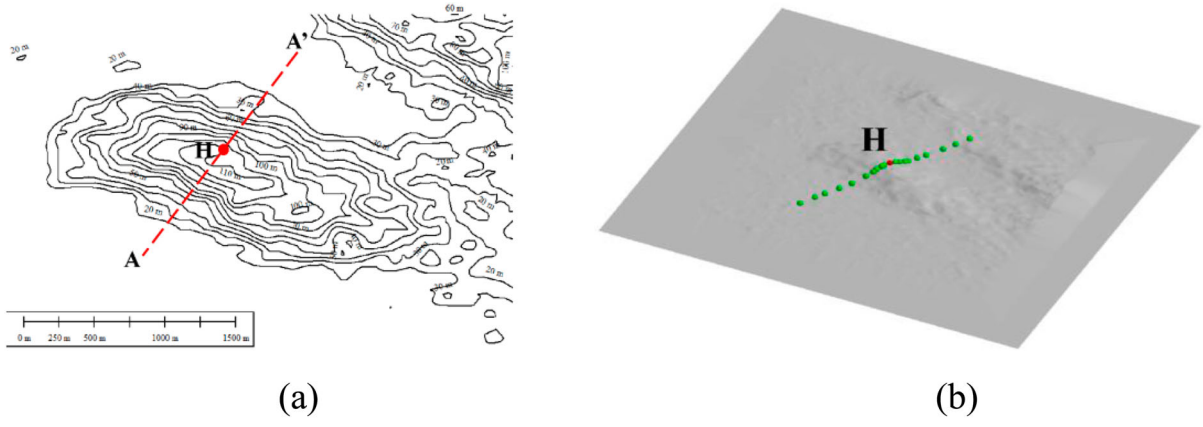

Figure 6. Position of measuring points. (a) Measuring points on the line A-A', (b) Measuring points in calculation.

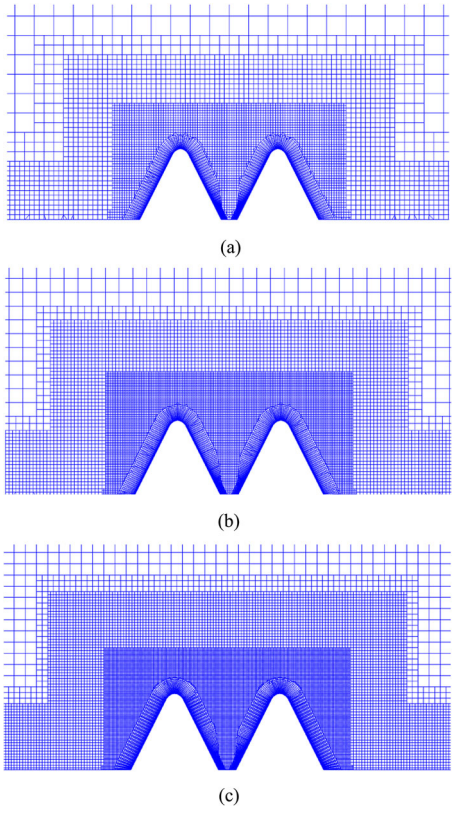

Figure 8. Three grid models with different grid resolutions. (a) Low resolution grid, (b) Medium resolution grid, (c) High resolution grid.

height of 250 metres above the ground, with a spacing of 2 metres, and their positions are shown in Figure 9. The wind speeds obtained from the three grid models under different resolutions are compared in Figure 10. It reveals that the wind speed distributions are generally consistent. However, the wind speed at the measurement points in the low-resolution grid model is slightly lower than that in the other two models. To ensure the accuracy of the solution and reduce computational cost, the

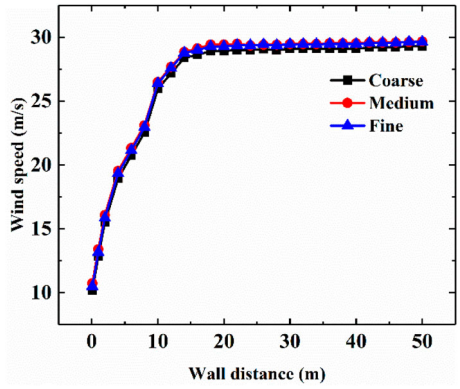

Figure 10. Comparison of the wind speeds under three grid models.

medium-resolution grid model was selected for subsequent calculations.

4. Results and discussion

4.1. Wind field characteristics

In this section, we focus on the analysis of wind field characteristics. Since the lateral wind load has the most significant impact on the stability of the train, we will be discussing the y-direction velocity components. At the entrance of the gorge, we define the y-coordinate as 0, and in Figure 11, we present the velocity contours of the cross-section with varying y-coordinate values. It can be observed that the airflow at the entrance of the gorge is partially accelerated towards the middle due to the obstruction of the mountain. Meanwhile, the airflow in the middle of the gorge is slower, influenced by the ground boundary layer. As a result, high winds are present on both sides, and a low wind speed zone exists in the middle of the gorge, as indicated by the black dashed boxes in the figure. As we move towards the back of the gorge, the low wind speed zone gradually

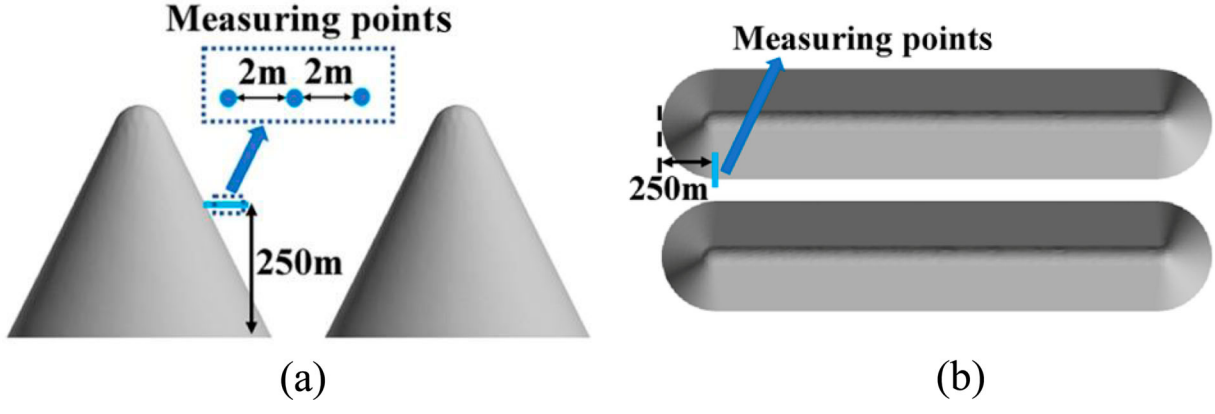

Figure 9. Position of measuring points. (a) Front view, (b) Vertical view.

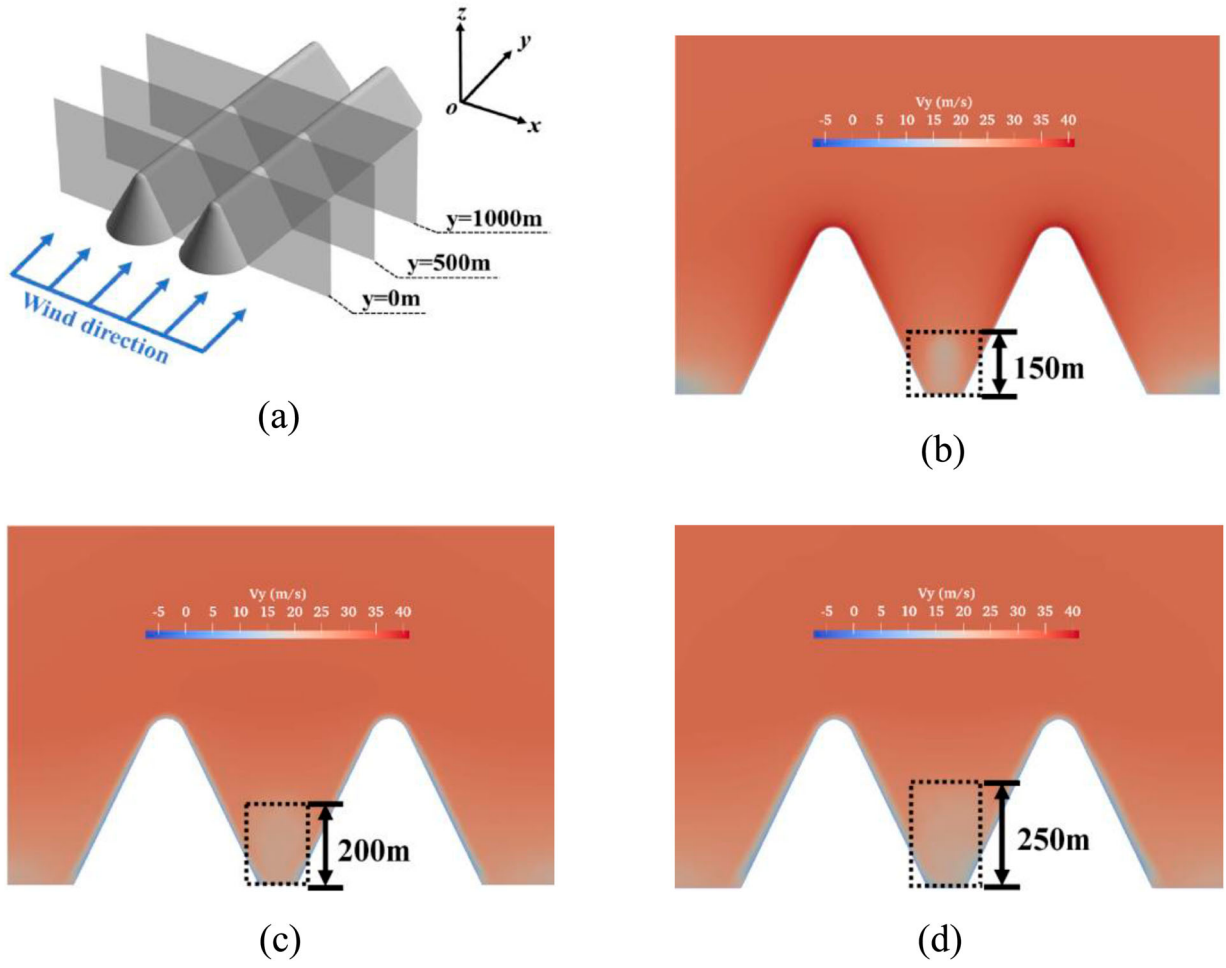

Figure 11. Sections' location and velocity contours in y direction. (a) Location of the sections along the y-axis, (b) Velocity contour (y = 0 m), (c) Velocity contour (y = 500 m), (d) Velocity contour (y = 1000 m).

expands, and after stabilization, it extends up to 250 m, which is approximately 56% of the gorge height. The influence of gorge topography on wind speed distribution is evident as the airflow at the bottom of the entire gorge is obstructed and flows at a lower velocity, providing guidance for site selection of bridge and building construction.

Figure 12 shows velocity contours for three planes in the z-direction. As shown in the figure, the velocity on both sides of the mountain is bigger, especially in the area where the airflow from the front of both mountains converges and flows into the gorge. The curved shape of the mountain front reduces the flow area, leading to an increase in wind speed at the entrance of the gorge. The maximum wind speed occurs at the end of the circular arc segment, indicating that there is a zone of wind speed acceleration at the entrance. Due to the ground's obstruction to airflow, the wind speed in the middle of the wind speed acceleration zone decreases at lower heights. However, at higher heights, the obstruction of airflow by the ground decreases, resulting in a reduction of the low wind speed zone in the middle of the wind speed acceleration zone.

The monitoring of wind velocity and observation of velocity contours reveal the existence of a velocity boundary layer on the mountain's surface. The wind speed at the wall is zero, and it gradually increases with the distance from the wall. In addition, the roughness height of the wall disturbs the airflow, making the velocity boundary layer on the mountain wall more distinct. Figure 13 shows the boundary layer at different y-coordinates on the mountain wall. As shown in the figure, the thickness of the velocity boundary layer is small at the entrance of the gorge and gradually increases to a certain value before remaining constant as the airflow moves into the gorge. For high-speed trains, the distribution of wind speed along the direction of train travel is crucial for safe operation in the gorge area. As the train passes through the gorge, it crosses the velocity boundary layer on the walls of the two mountains. In the subsequent section, we will develop and scrutinize the mathematical model of the wind field within the boundary layer of the gorge.

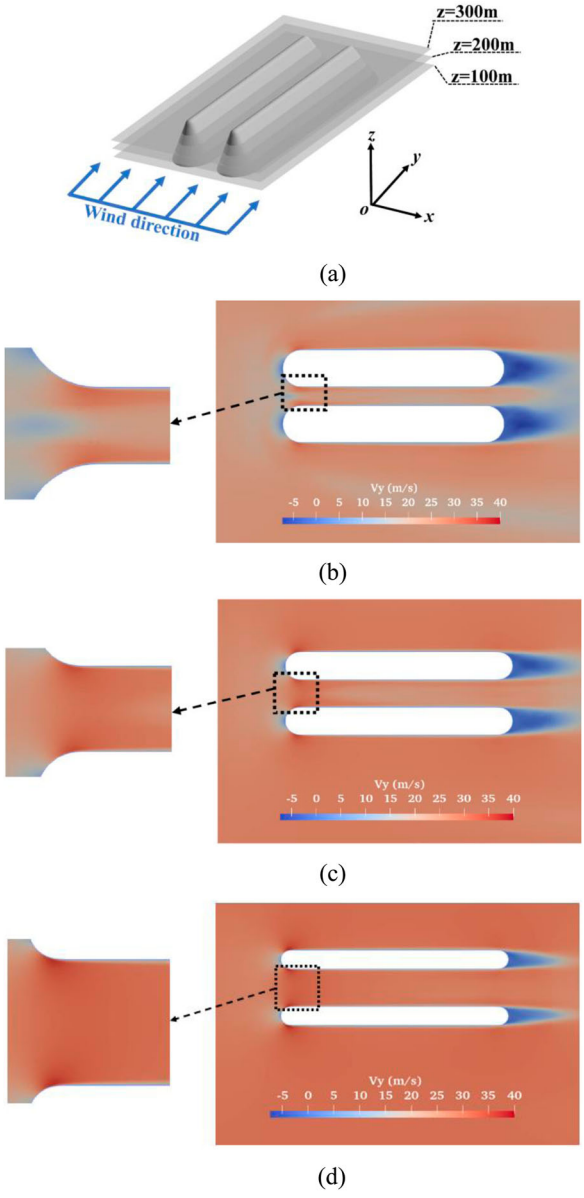

Figure 12. Sections' location and velocity contours in z direction. (a) Location of the sections along the z-axis, (b) Velocity contour (z = 100 m), (c) Velocity contour (z = 200 m), (d) Velocity contour (z = 300 m).

4.2. Mathematical model of gorge wind

Taking the cross-section of y = 200 m as an example to study the wind field model in the gorge, the measurement points are spaced 50 m apart at different heights between 50 and 450 m, with the measurement point closest to the mountain wall being 0.1 m away from the wall and the interval between each measurement point along the x-direction being 2 m. The algorithm outlined in the previous section is used to determine the average wind speed at each measurement point. Figure 14 displays the position of the measurement spots as well as the wind speed at those points. The velocity boundary layer near the mountain wall exists, as can be seen from the distribution of wind speed at measurement points at various heights. The wind speed increases gradually from small to large with increasing horizontal distance from the wall, and the maximum value of wind speed at measurement points at various heights also rises gradually with increasing height. The low wind speed interval, which is detailed in section 4.1, is the range below the height of 250 m where the wind speed of the measurement locations along the x-direction climbs to a particular value and then progressively falls.

The distribution of wind speed in the vertical direction of the gorge is described by Equation (14), which employs an expression similar to that of the exponential wind in the surface boundary layer. Here, h represents the height of the mountain, z is the coordinate in the vertical direction, U_h denotes the wind speed at the mountain's highest point, and α_1 is the wind speed increase index in the height direction. This equation helps to illustrate the distribution of maximum wind speed at different heights inside the gorge. The mountain's height and wind speed at its peak are considered known characteristics, as we are primarily interested in studying the wind field within the gorge.

$$U(z) = U_h\left(\frac{z}{h}\right)^{\alpha_1} \tag{14}$$

Analogous to the increase in wind speed with height, an exponential expression is adopted to depict the variation of wind speed in the horizontal direction. As demonstrated in Equation (15), U_{max} represents the maximum wind speed at a specific height in Equation (14). In addition, x_0 represents the interval of wind speed growth along the horizontal direction near the mountain wall. Within the distance less than x_0 from the wall, wind speed gradually increases. In the process of determining x_0, we set a threshold such that when the wind speed at a measuring point reaches 95% of the maximum wind speed at the height of the measuring point. The distance from that point to the wall is considered to be the x_0. Moreover, α_2 signifies the wind speed growth index in horizontal direction.

$$U(x) = U_{max}\left(\frac{x}{x_0}\right)^{\alpha_2} \tag{15}$$

To model the wind profile across the entire gorge, the wind profiles at multiple cross-sections are combined. Specifically, the two-dimensional model of gorge wind can be obtained by combining Equation (14) and Equation (15), which describe the vertical and horizontal variations of wind speed, respectively, for a specific cross-section in the gorge. The resulting model is expressed as Equation (16), in which the values of the three parameters, namely, x_0, α_1, and α_2, are determined based on the

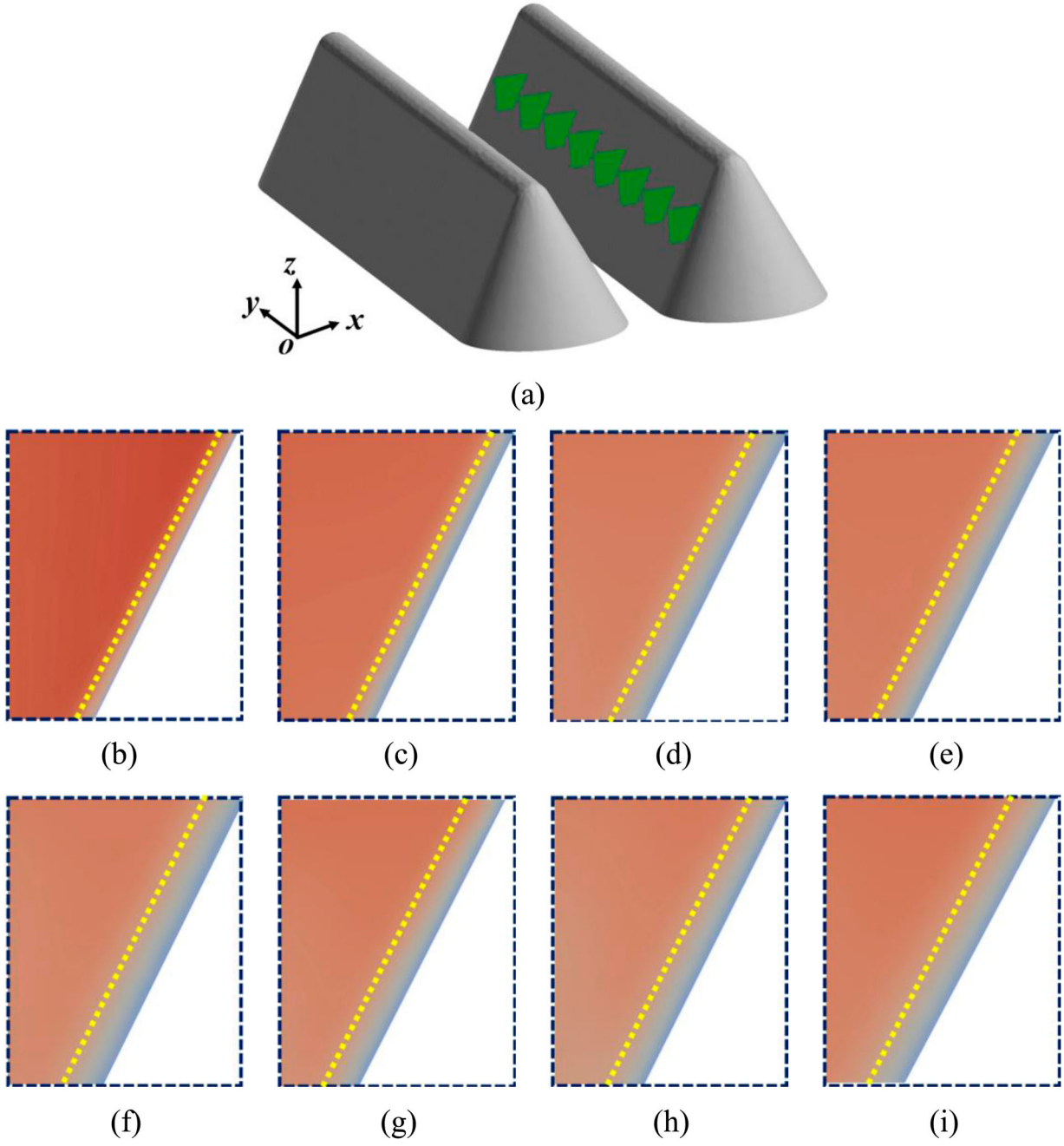

Figure 13. Velocity boundary layer at sections of the mountain slope along the y-axis. (a) Location of the sections, (b) y = 0 m, (c) y = 250 m, (d) y = 500 m, (e) y = 750 m, (f) y = 1000 m, (g) y = 1250 m, (h) y = 1500 m, (i) y = 1750m.

calculated wind speed data. This two-dimensional model provides a useful tool for predicting the wind speed and direction in the gorge, which is important for many practical applications, such as wind energy development and air pollution dispersion.

$$U(x,z) = \mathrm{U_h}\left(\frac{z}{\mathrm{h}}\right)^{\alpha_1}\left(\frac{x}{\mathrm{x_0}}\right)^{\alpha_2} \tag{16}$$

We analyzed the wind speed on only one side of the gorge because both sides of the gorge are symmetrical and have an identical wind speed growth interval near the mountain. Figure 15 shows the location of the measurement points and the corresponding wind speeds. The measurement points are 50 metres away from the wall. At the cross-section of y = 200 m, x_0 is approximately 15 m because the wind speed primarily increases by 15 m in the vertical direction. It is worth noting that the mountain's height is 450 m, which means that the boundary layer effect near the summit is reduced. Consequently, the wind speed increase rate at this height differs from that at

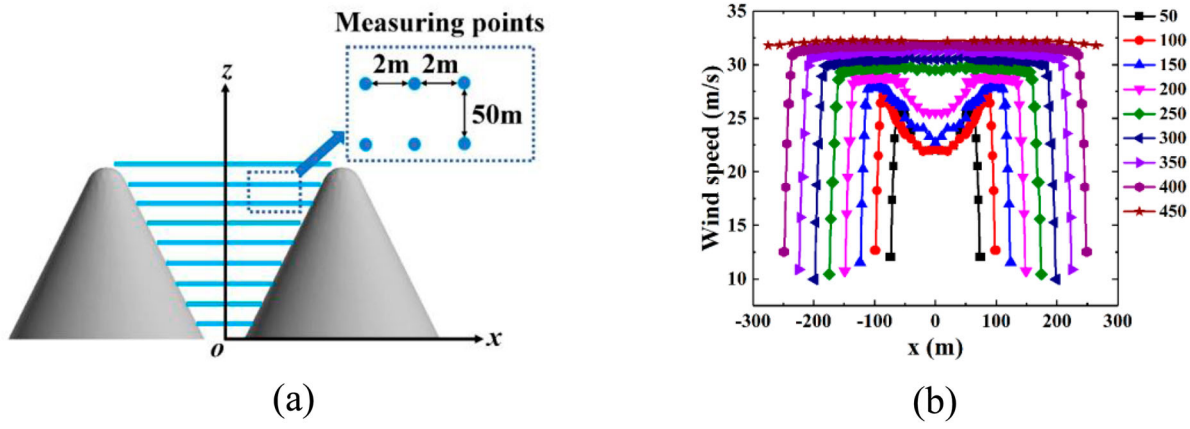

Figure 14. Wind speed of measuring points. (a) Position of measuring points, (b) Wind speed of measuring points.

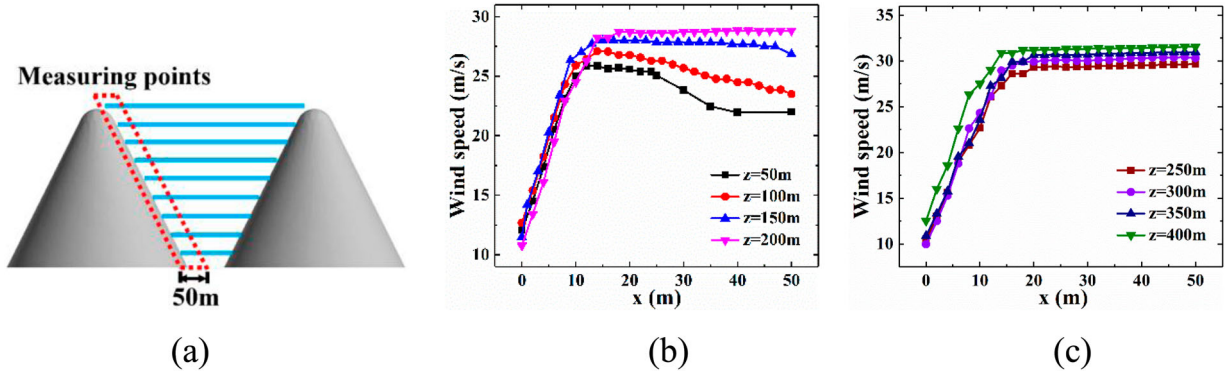

Figure 15. Wind speed of measuring points at different heights. (a) Position of measuring points, (b) Wind speed of measuring points(z = 50m-200 m), (c) Wind speed of measuring points(z = 250m-400 m).

other heights, and therefore, x_0 analysis does not apply to this height.

After determining the wind speed growth interval near the mountain wall at x_0, we identified the maximum wind speed at each height within the x_0 interval, corresponding to the measurement location 50 metres away from the wall. Next, we fitted this data to Equation (14), where the dependent variable is U/U_h (where U_h represents the maximum wind speed at a height of 450 m) and the independent variable is z/h (where z indicates the height and z = 0 at the bottom of the gorge). The fitting results are illustrated in Figure 16.

For the y = 200 m cross-section, the fitted value of parameter α_1 was approximately 0.11 with an interval of ±0.006, the coefficient of determination was roughly 0.95. The exponent α_1 in the gorge wind model is similar to the roughness exponent in the atmospheric boundary layer wind model, which reflects the influence of the surface on the growth rate of wind speed with height. A smaller value of α_1 indicates a faster increase in speed with height. Comparing the results with Table 2 reveals that the growth exponent near the gorge entrance is slightly smaller than the roughness exponent of class A surfaces, indicating a faster increase in wind speed with height at the gorge entrance.

The wind speed at the measurement points within 15 m from the mountain surface at different heights is fitted in the form of Equation (15) with U/U_{max} as the dependent variable (here U_{max} is the wind speed at the measurement point at 15 m in x coordinate) and x/x_0 as the independent variable (here x is the distance from the mountain wall to the measurement point), the α_2 values at heights from 100 m to 400 m and the coefficients of determination are shown in Table 4. As Table 4 shows, the values of α_2 in the cross-section of y = 200 m are about 0.29 to 0.48, and the coefficients of determination are above 0.93. The parameter α_2 reflects the rate of horizontal wind speed growth. The airflow at the middle position of the canyon is affected by the boundary layer of the mountain walls at both ends in the horizontal direction, while only influenced by the ground in the vertical direction. Therefore, the growth factor of horizontal wind speed α_2 is greater than the growth factor of vertical wind speed α_1.

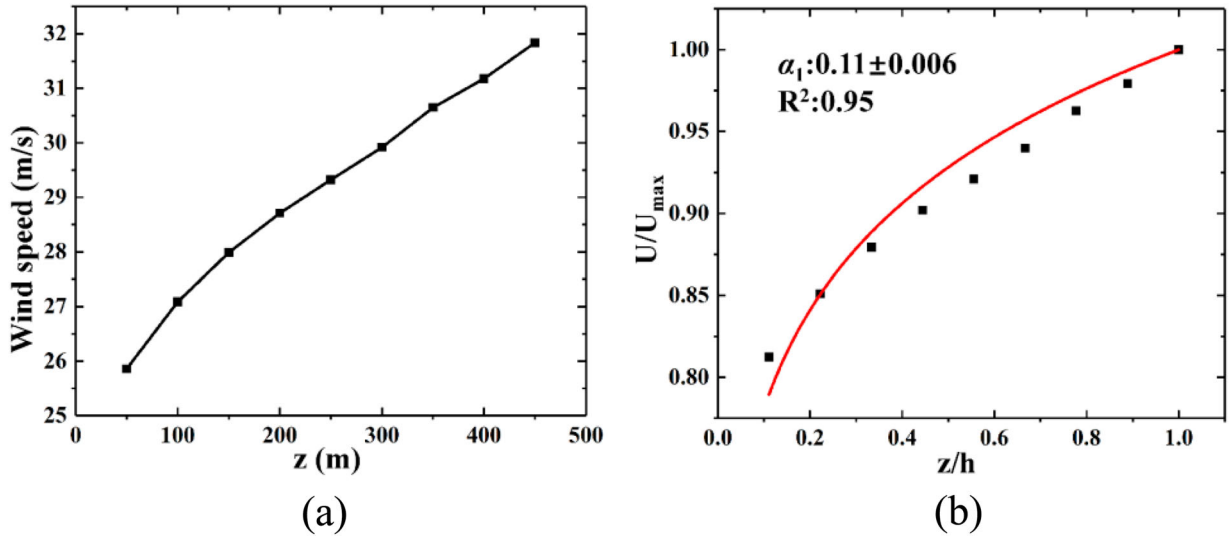

Figure 16. Parameter α_1 fitting. (a) Wind speed on different heights, (b) Wind speed fitting,.

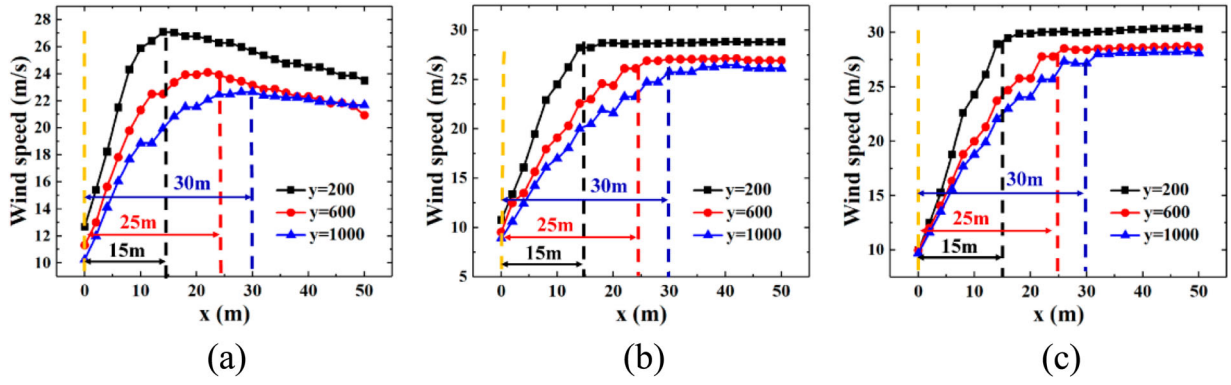

Figure 17. Comparison of parameter x_0 of different sections along the z-axis. (a) Wind speed at z = 100 m, (b) Wind speed at z = 200 m, (c) Wind speed at z = 300 m.

Table 4. The fitted α_2 and the fitted determination coefficient of y = 200 m cross-section.

Heights	α_2	Interval	R^2
100 m	0.29	**±0.026**	0.94
150 m	0.35	**±0.025**	0.96
200 m	0.41	**±0.021**	0.98
250 m	0.46	**±0.030**	0.96
300 m	0.47	**±0.024**	0.98
350 m	0.48	**±0.033**	0.95
400 m	0.37	**±0.021**	0.97

According to the flow field analysis in 4.1, there is an obvious difference between the flow state at the entrance of the gorge and the middle position of the gorge. In order to examine the difference of the parameters of the wind field model at different longitudinal depths of the gorge, the same wind field model study was conducted for the longitudinal 1/4 depth of the gorge (y = 600 m) and the middle depth of the gorge (y = 1000 m). Give the wind velocities at three cross-sections at 100, 200 and 300 m height for example of the measuring points within 50 m near the wall, as shown in Figure 17. It is clear that x_0 at y = 600 m cross-section is approximately 25 metres, and x_0 at y = 1000 m cross-section is approximately 30 metres, indicating that the wind speed at the entrance of the gorge near the wall grows faster and the thickness of the velocity boundary layer is thinner, which is similar to the flat boundary layer. As the boundary layer's development length increases, the thickness of the layer gradually rises to a certain value and stabilizes.

After obtaining x_0 from cross-sections at different y-values, the wind speed at the measured point at x_0 from the wall in the horizontal direction on the two cross-sections was fitted with Equation (14) to obtain the parameter α_1 of the wind field model, as shown in Figure 18. Comparing with α_1 at the entrance of the gorge in the previous paper, the value of α_1 gradually increases as the position of the cross-section moves away from the entrance of the gorge. These results indicate that the wind speed at the gorge's entrance increases with height more quickly than it does in the middle of the gorge because

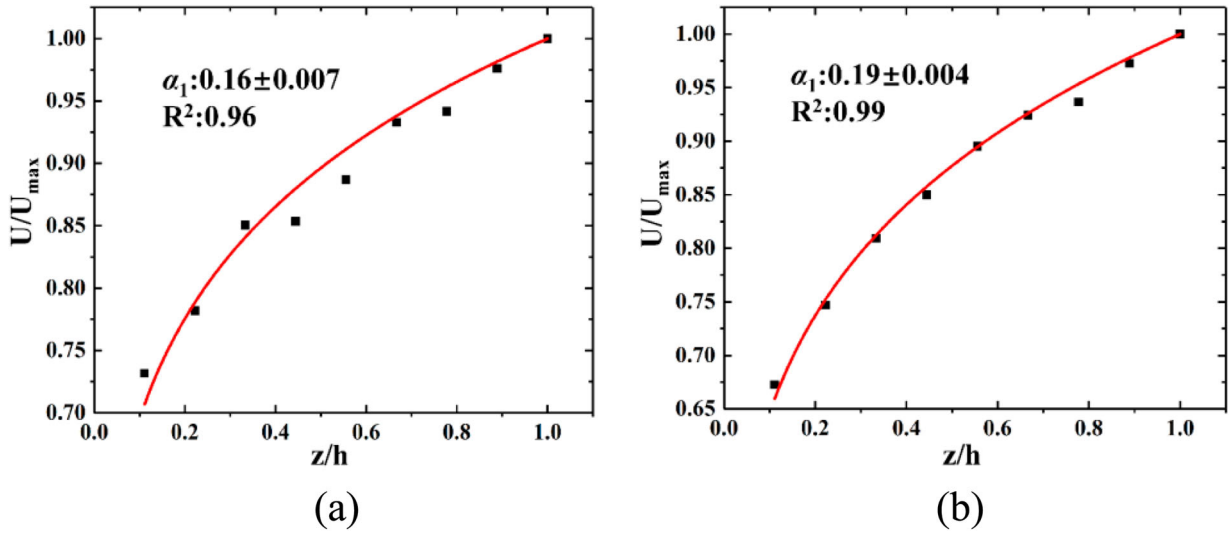

Figure 18. Comparison of parameter α_1 of different sections along the y-axis. (a) Wind speed fitting (y = 600 m), (b) Wind speed fitting (y = 1000 m).

Table 5. The fitted α_2 and the fitted determination coefficient of y = 600 m cross-section.

Heights	α_2	Interval	R^2
100 m	0.21	**±0.018**	0.91
150 m	0.30	**±0.017**	0.96
200 m	0.37	**±0.011**	0.99
250 m	0.41	**±0.017**	0.97
300 m	0.38	**±0.012**	0.99
350 m	0.37	**±0.013**	0.98
400 m	0.29	**±0.014**	0.97

Table 6. The fitted α_2 and the fitted determination coefficient of y = 1000 m cross-section.

Heights	α_2	Interval	R^2
100 m	0.22	**±0.012**	0.95
150 m	0.29	**±0.013**	0.97
200 m	0.37	**±0.010**	0.99
250 m	0.40	**±0.015**	0.97
300 m	0.36	**±0.009**	0.99
350 m	0.34	**±0.010**	0.98
400 m	0.27	**±0.014**	0.96

the boundary layer between the ground and mountains has less of an impact there. As the wind blows deeper into the gorge, however, the airflow becomes more and more influenced by the boundary layer, and the increase in wind speed in the height direction gradually slows down.

Equation (15) was used to fit the wind speed at the measuring stations within x_0 of the mountain's surface on the cross sections of y = 600 m and y = 1000 m. The results are displayed in Tables 5 and 6 as values for α_2 and decision coefficients at various heights for the two cross-sections. As shown in the tables, the values of α_2 at the gorge's entrance are higher than the values of α_2 at its middle location at various heights, indicating that the rate of increase in wind speed at the gorge's entrance near the mountain wall is slower than at the middle location of the gorge.

4.3. Influence of gorge parameters on wind field model parameters

Considering the gorge width (equivalent to the bridge length) as an important parameter in practical engineering applications, the wind fields of gorges of different widths were calculated, and data from the entrance of the gorge and the middle section of the gorge were selected to compare the effect of the gorge width on the wind field model parameters. Firstly, the effect of gorge width on the thickness of the velocity boundary layer near the mountain wall, i.e. the size of x_0, was compared. Wind speeds at measuring points within 50 m from the wall in the horizontal direction were measured at heights of 100, 200, and 300 m, and the results are shown in Figures 19–21. As depicted in the figures, the effect of gorge width on the thickness of the velocity boundary layer of the mountain wall is small, and the thickness of the velocity growth interval near the mountain wall under different width conditions is basically the same.

The parameters of the wind field model for gorges of different widths were fitted by adopting the treatment of 4.1, and the values of α_1 and α_2 were obtained for different cross-sections in the gorges at three widths. The parameters α_1 and α_2 in the wind field models for gorges of different widths were compared.

As Figures 22 shows, the values of α_1 are almost the same for different gorge widths at the entrance of the gorge, in the other two cross-sections, α_1 decreases with the increase of gorge width. This is due to the fact that at the entrance of the gorge, the velocity growth in the

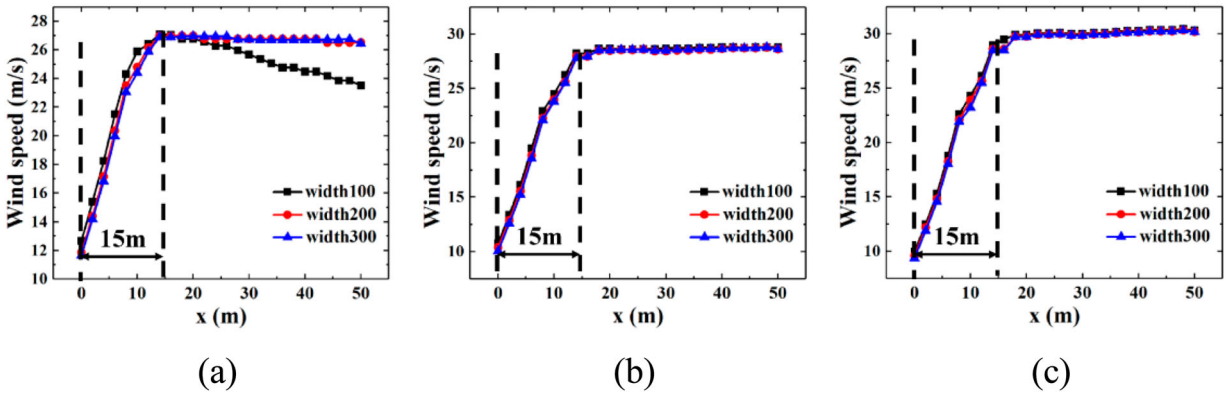

Figure 19. Comparison of parameter x_0 of different gorge widths at section y = 200 m. (a) Wind speed at z = 100 m, (b) Wind speed at z = 200 m, (c) Wind speed at z = 300 m.

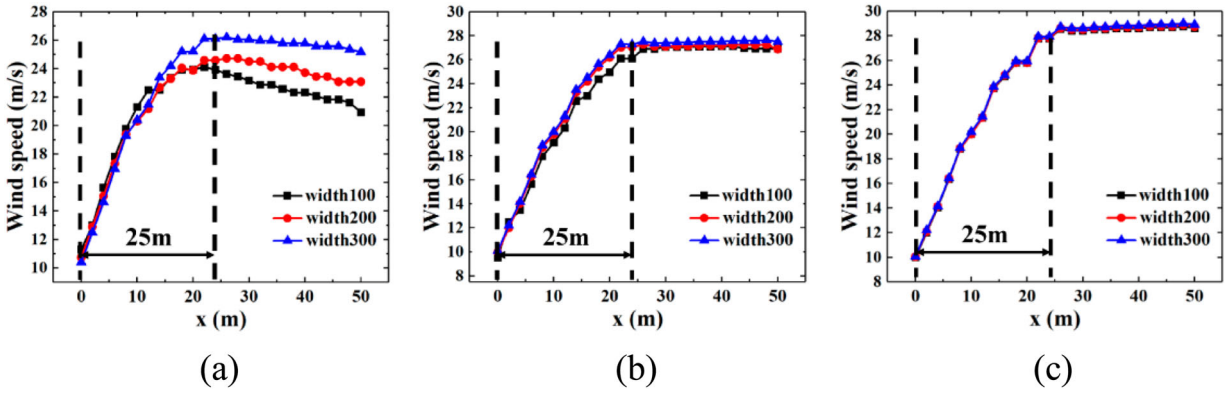

Figure 20. Comparison of parameter x_0 of different gorge widths at section y = 600 m. (a) Wind speed at z = 100 m, (b) Wind speed at z = 200 m, (c) Wind speed at z = 300 m.

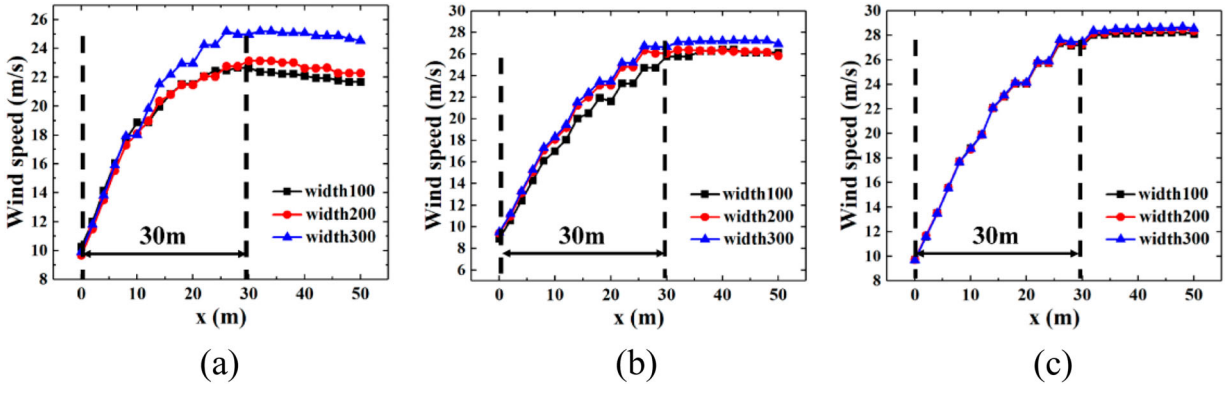

Figure 21. Comparison of parameter x_0 of different gorge widths at section y = 1000 m. (a) Wind speed at z = 100 m, (b) Wind speed at z = 200 m, (c) Wind speed at z = 300 m.

height direction has not been affected by the boundary layer of the ground and the mountain wall, the maximum velocity at various heights is mainly related to the incoming flow boundary conditions, the width of the gorge has less influence on the velocity growth in height. In the cross-sections of y = 600 m and y = 1000 m, the gorge width affects the velocity distribution near the ground, the wider gorge it is, the less influence on the velocity distribution near the ground by the boundary layer and the higher wind speed, so the smaller α_1 value obtained from the fit.

As Figure 23 shows, the situation of α_2 is different from α_1 at the entrance of the gorge, with the increase of gorge width α_2 are slightly increased, this is because α_2 characterizes the wind speed growth rate within the boundary layer of the mountain wall in the horizontal direction, with the increase of width, the wind speed growth effect at the entrance of the gorge is weakened,

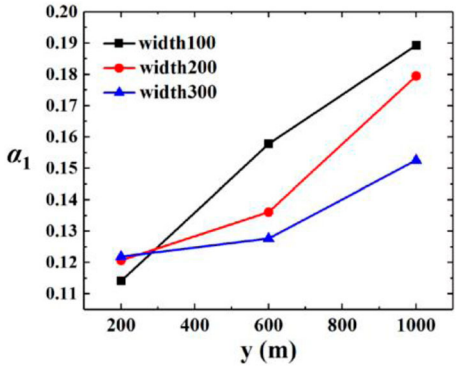

Figure 22. Comparison of parameter α_1 of different gorge widths.

so the wind speed growth rate within the boundary layer of the wall decreases, hence α_2 decreases. As the cross-sectional position moves deeper in the gorge, the effect of gorge width on α_2 gradually decreases, above the height of 250 m, the gorge width has almost no effect on α_2, at a height of 100 m, α_2 decreases with the increase of gorge width, due to the lower velocity at lower heights caused by the combined influence of the ground and the mountain surface's boundary layer, and with the increase of the gorge width, the obstructive effect of the boundary layer on the airflow movement is weakened, so the velocity at the mountain surface increases and the value of α_2 decreases. There is no discernible change in the values of α_2 at different gorge widths at higher altitudes because the region below the mountain surface's boundary layer is largely open and the gorge's width has less of an impact on the wind speed there.

5. Conclusions

This paper established a two-dimensional mathematical model of the gorge wind field by verifying the accuracy of the numerical simulation algorithm and grid through comparison with measured data. The wind field inside a typical gorge was then calculated, and the impact of the gorge's width on the model parameters was examined. Based on the analysis, the following conclusions were drawn:

The wind speed at the entrance of the gorge increases due to the constriction of the flow path area. Inside the gorge, the wind speed is affected by the ground and mountain boundary layer, resulting in a low wind speed zone below 250 m. Additionally, a velocity boundary layer exists on the surface of the mountain. Its thickness is relatively small at the entrance of the gorge, but it gradually increases and becomes stable with the development length of the airflow in the gorge.

A two-dimensional model of the wind field in the gorge was established, with the parameter x_0 denoting the thickness of the velocity boundary layer on the mountain wall in the horizontal direction. The thickness of this layer is about 15 m at the entrance of the gorge and increases to around 30 m at the middle position. The parameter α_1 represents the index of velocity growth in the height direction, which increases gradually from 0.11 to 0.19 as the position moves from the entrance to the middle of the gorge. The parameter α_2 represents the index of velocity growth in the horizontal direction, with the value of α_2 being slightly larger at the entrance than at the middle position of the gorge.

The parameter x_0 remained relatively constant regardless of the gorge width. As for the parameter α_1, it remained unchanged at the entrance of the gorge but decreased as the gorge widened, after the airflow had entered the gorge for some time. Conversely, the parameter α_2 slightly increased with the gorge width at the entrance, while in the middle of the gorge, at a height greater than 250 m, α_2 remained mostly constant, and only increased with the gorge width at a height of 100 m.

The numerical simulation in this study used an appropriate grid resolution and a simplified typical gorge model, which differs from the actual mountainous gorge.

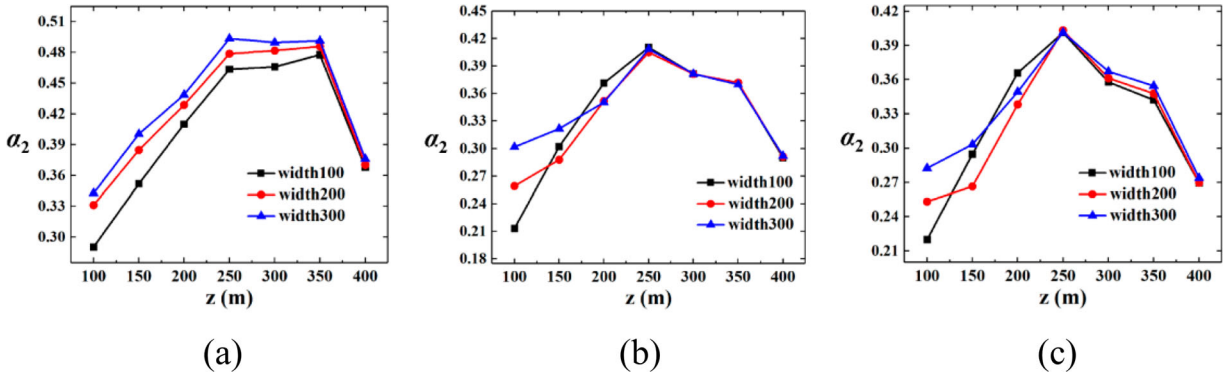

Figure 23. Comparison of parameter α_2 of different gorge widths. (a) α_2 at different heights (y = 200 m), (b) α_2 at different heights (y = 600 m), (c) α_2 at different heights (y = 1000 m).

While the calculated wind speed results may have some differences from the real-world situation, they still reflect wind field characteristics. The proposed wind field model can reveal the distribution pattern of wind fields in typical gorges. Determining specific parameters and how they vary with gorge features requires further numerical simulations and experiments at different scales. In the future, we will conduct wind tunnel experiments to verify the model parameters, and apply the proposed wind field model in the study of high-speed train operation stability.

Disclosure statement

No potential conflict of interest was reported by the author(s).

Funding

This work was supported by National Natural Science Foundation of China under Grant 52172336; and China National Railway Group Science and Technology Program under Grant N2022T001.

References

Abdi, D., & Bitsuamlak, G. (2014). Wind flow simulations on idealized and real complex terrain using various turbulence models. *Advances in Engineering Software*, *75*, 30–41. https://doi.org/10.1016/j.advengsoft.2014.05.002

Blocken, B., Stathopoulos, T., & Carmeliet, J. (2007). CFD simulation of the atmospheric boundary layer: Wall function problems. *Atmospheric Environment*, *41*(2), 238–252. https://doi.org/10.1016/j.atmosenv.2006.08.019

Cebeci, T., & Bradshaw, P. (1977). *Momentum transfer in boundary layer*. Hemisphere Pub. Corp.

Chen, X. (2022). Research on wind characteristics of typical canyon terrain and its influence on the flow field of different cross-section forms. [Master's thesis, Chang'an University].

Davenport, A. (1962). The spectrum of horizontal gustiness near the ground in high winds. *Quarterly Journal of the Royal Meteorological Society*, *88*(376), 197–198. https://doi.org/10.1002/qj.49708837618

Deng, Y., Liu, S., Yu, Z., & Zeng, X. (2010). Analysis of the impact of roughness on CFD simulation of actual terrain wind fields. *Acta Energiae Solaris Sinica*, *31*(12), 1644–1648.

Di, Z., Li, Y., & Liao, H. (2017). Effect of ground surface roughness on wind field over bridge site with a gorge in mountainous area. *Engineering Mechanics*, *34*(6), 73–81. https://doi.org/10.6052/j.issn.1000-4750.2015.12.0970

He, J., Xiang, H., Li, Y., & Han, B. (2022). Aerodynamic performance of traveling road vehicles on a single-level rail-cum-road bridge under crosswind and aerodynamic impact of traveling trains. *Engineering Applications of Computational Fluid Mechanics*, *16*(1), 335–358. https://doi.org/10.1080/19942060.2021.2012516

Hong, F. (2020). *Study on wind characteristics of V and U-shaped mountain canyon bridge site.* [Master's thesis, Shijiazhuang Tiedao University].

Kaimal, J. C., Wyngaard, J. C., Izumi, Y., & Coté, O. R. (1972). Spectral characteristics of surface-layer turbulence. *Quarterly Journal of the Royal Meteorological Society*, *98*(417). https://doi.org/10.1002/qj.49709841707

Ke, Y., & Pei, C. (2022). Measured research on the characteristics of wind field at the U-shaped canyon bridge in the western mountainous area. *Shanxi Architecture*, *48*(17), 169–172. https://doi.org/1009-6825.2022.17.044

Li, Y., Cai, X., Tang, K., & Liao, H. (2011). Study of spatial distribution feature of wind field over bridge site with a deep-cutting gorge using numerical simulation. *China Civil Engineering Journal*, *44*(2), 116–122. https://doi.org/10.15951/j.tmgcxb.2011.02.004

Li, Y., Di, Z., Wang, B., & Liao, H. (2016). Numerical simulation of wind characteristics over bridge site near y-shaped river junction in mountainous area. *Journal of Southwest JiaoTong University*, *51*(2), 341–348. https://doi.org/10.3969/j.issn.0258-2724.2016.02.013

Li, Y., Tang, K., Cai, X., & Liao, H. (2010). Integrated wind speed standard for long-span bridge over deep-cutting gorge. *Journal of Southwest Jiaotong University*, *45*(2), 167–173. https://doi.org/10.3969/j.issn.0258-2724.2010.02.001

Li, Z., Xu, S., Xiao, Z., & Zhou, D. (2016). Detailed interpolation of hilly wind topographic factor along hillside. *Journal of Hunan University (Natural Sciences)*, *43*(3), 23–31. https://doi.org/10.3969/j.issn.1674-2974.2016.03.004

Mao, J., Xi, Y., & Yang, G. (2011). Research on influence of characteristics of cross wind field on aerodynamic performance of a high-speed train. *Journal of The China Railway Society*, *33*(4), 22–30. https://doi.org/10.3969/j.issn.1001-8360.2011.04.004

Menter, F. (1994). Two-equation eddy-viscosity turbulence models for engineering applications. *Aiaa Journal*, *32*(8), https://doi.org/10.2514/3.12149

Murakami, S. (1993). Comparison of various turbulence models applied to a bluff body. *Journal of Wind Engineering & Industrial Aerodynamics*, *s 46–47*(none), 21–36. https://doi.org/10.1016/0167-6105(93)90112-2

Pang, J., Song, J., & Lin, Z. (2010). Field measurement analysis of wind turbulence characteristics of sidu river valley bridge site. *China Journal of Highway and Transport*, *23*(3), 42–47. https://doi.org/10.3969/j.issn.1001-7372.2010.03.007

Pattanapol, W., Wakes, S. J., Hilton, M. J., & Dickinson, K. (2007). Modeling of surface roughness for flow over a complex vegetated surface. *International Journal of Mathematical Physical & Engineering S*, *1*, 18.

Shen, L., Hua, X., Han, Y., Cai, C., & Wei, C. (2020). Numerical simulation of wind field at canyon bridges with high precision inlet boundary. *China Journal of Highway and Transport*, *33*(07), 114–123. https://doi.org/10.19721/j.cnki.1001-7372.2020.07.012

Tan, B. (2019). *Field measurement of wind properties at a bridge site near a canyon deep-cut to hilly land* [Doctoral dissertation, Hunan University].

Tang, Y., Zheng, S., Zhao, B., & Li, M. (2014). Numerical investigation on the self-sustaining of equilibrium atmosphere boundary layers. *Engineering Mechanics*, *31*(10), 129–135. https://doi.org/10.6052/j.issn.1000-4750.2013.04.0376

Taylor, P., & Teunissen, H. (1985). *The Askervein hill project: report on the September/October 1983, main field experiment*.

Taylor, P., & Teunissen, H. (1987). The Askervein hill project: Overview and background data. *Boundary-Layer Meteorology*, *39*(1-2), 15–39. https://doi.org/10.1007/BF00121863

Wieringa, J. (1992). Updating the davenport roughness classification. *Journal of Wind Engineering & Industrial Aerodynamics*, *41*(1–3), 357–368. https://doi.org/10.1016/0167-6105(92)90434-C

Xia, Y., Liu, T., Su, X., Jiang, Z., Chen, Z., & Guo, Z. (2022). Aerodynamic influences of typical windbreak wall types on a high-speed train under crosswinds. *Journal of Wind Engineering and Industrial Aerodynamics*, *231*, 105231. https://doi.org/10.1016/j.jweia.2022.105231

Xue, Y., & Liu, Z. (2016). Numerical simulation of spatial distribution feature of wind field over bridge site at complex terrain. *Journal of Highway and Transportation Research and Development*, *33*(5), 66–72. https://doi.org/10.3969/j.issn.1002-0268.2016.05.011

Yang, W., Deng, E., He, X., Luo, L., Zhu, Z., Wang, Y., & Li, Z. (2021). Influence of wind barrier on the transient aerodynamic performance of high-speed trains under crosswinds at tunnel–bridge sections. *Engineering Applications of Computational Fluid Mechanics*, *15*(1), 727–746. https://doi.org/10.1080/19942060.2021.1918257

Zhang, J., Zhang, M., Li, Y., Jiang, F., & Guo, D. (2021). Comparison of wind characteristics in different directions of deep-cut gorges based on field measurements. *Journal of Wind Engineering and Industrial Aerodynamics*, *212*(2021), 104595. https://doi.org/10.1016/j.jweia.2021.104595

Zhang, S., Guo, J., & Dai, L. (2017). Determination of design wind parameters for qingshuihe bridge. *Journal of Traffic and Transportation Technology*, *13*(7), 221–223.

Zhao, Y. (2021). *Experimental study on wind field characteristics of typical landforms in complex mountainous*. [Master's thesis, Shijiazhuang Tiedao University].

Zhou, D., Tian, H., Yang, M., & Lu, Z. (2008). Comparison of aerodynamic performance of passenger train traveling on different railway conditions up strong cross-wind. *Journal of Central South University (Science and Technology)*, *39*(3), 554–559.

Zhou, D., Yu, D., Wu, L., & Meng, S. (2023). Numerical investigation of the evolution of aerodynamic behaviour when a high-speed train accelerates under crosswind conditions. *Journal of Wind Engineering and Industrial Aerodynamics*, *72*, 51–56. https://doi.org/10.1016/j.aej.2023.03.064

Zou, S., He, X., & Wang, H. (2022). Numerical simulation of the influences of wind barriers on aerodynamic characteristics of trains on bridge and bridges. *China Railway Science*, *43*(05), 51–59.